Plant Cell Reports (2025) 44:115
https://doi.org/10.1007/s00299-025-03498-7

ORIGINAL ARTICLE

Distinct actin microfilament localization during early cell plate formation through deep learning-based image restoration

Suzuka Kikuchi[1] · Takumi Kotaka[2] · Yuga Hanaki[3] · Minako Ueda[3] · Takumi Higaki[2,4,5]

Received: 16 February 2025 / Accepted: 8 April 2025

Abstract

Key message **Using deep learning-based image restoration, we achieved high-resolution 4D imaging with minimal photodamage, revealing distinct localization and suggesting Lifeact-RFP-labeled actin microfilaments play a role in initiating cell plate formation.**

Abstract Phragmoplasts are plant-specific intracellular structures composed of microtubules, actin microfilaments (AFs), membranes, and associated proteins. Importantly, they are involved in the formation and the expansion of cell plates that partition daughter cells during cell division. While previous studies have revealed the important role of cytoskeletal dynamics in the proper functioning of the phragmoplast, the localization and the role of AFs in the initial phase of cell plate formation remain controversial. Here, we used deep learning-based image restoration to achieve high-resolution 4D imaging with minimal laser-induced damage, enabling us to investigate the dynamics of AFs during the initial phase of cell plate formation in transgenic tobacco BY-2 cells labeled with Lifeact-RFP or RFP-ABD2 (actin-binding domain 2). This computational approach overcame the limitation of conventional imaging, namely laser-induced photobleaching and phototoxicity. The restored images indicated that RFP-ABD2-labeled AFs were predominantly localized near the daughter nucleus, whereas Lifeact-RFP-labeled AFs were found not only near the daughter nucleus but also around the initial cell plate. These findings, validated by imaging with a long exposure time, highlight distinct localization patterns between the two AF probes and suggest that Lifeact-RFP-labeled AFs play a role in initiating cell plate formation.

Keywords Tobacco BY-2 cells · Phragmoplast · Actin microfilaments · Live-cell imaging · Image restoration · Deep learning

Introduction

The phragmoplast is a plant-specific intracellular structure that forms a cell plate to partition daughter cells during cytokinesis (Rasmussen et al. 2013; Smertenko et al. 2017). The backbone of the phragmoplast is made up of microtubules (MTs), which are involved in the assembly of the cell plate, together with actin microfilaments (AFs), membranes, and associated proteins (Müller and Jürgens 2016; Smertenko 2018). Proper formation and expansion of the phragmoplast is crucial for the completion of plant cytokinesis (Livanos and Müller 2019).

The formation and the expansion of the phragmoplast are regulated not only by MTs but also by the dynamics of AFs. MTs in the phragmoplast serve as essential tracks for the transport of vesicles to the division site, facilitating the construction of the cell plate during plant cytokinesis (Jürgens 2005). Previous studies on fixed or living cells have reported

Communicated by Peishan Yi.

✉ Takumi Higaki
thigaki@kumamoto-u.ac.jp

[1] Graduate School of Sciences and Technology for Innovation, Yamaguchi University, Yamaguchi, Japan

[2] Faculty of Science, Kumamoto University, Kumamoto, Japan

[3] Graduate School of Life Sciences, Tohoku University, Sendai, Japan

[4] Graduate School of Science and Technology, Kumamoto University, Kumamoto, Japan

[5] International Research Center for Agricultural and Environmental Biology, Kumamoto University, Kumamoto, Japan

that AFs exhibit MT-related dynamics and contribute to cell division by regulating cell plate expansion in plants. AFs specifically labeled with fluorescent phalloidin and/or monoclonal antibodies have been observed in fixed cells, including endosperm cells of *Haemanthus katherinae* (Schmit and Lambert 1987), root cells of *Allium cepa* (Clayton and Lloyd 1985), suspension culture cells of *Daucus carota* (Traas et al. 1987), suspension culture cells of *Medicago sativa* (Seagull et al. 1987), tobacco BY-2 cells (Kakimoto and Shibaoka 1987; Hasezawa et al. 1991), and suspension culture cells of *Arabidopsis thaliana* (Li et al. 2010). Although these traditional studies have provided valuable insights into AF localizations in plant cytokinesis, they have inherent limitations. Fixation eliminates temporal information, and transient events that occur over short timescales can only be detected infrequently. To address these issues, AFs labeled through the microinjection of fluorescent phalloidin or expression of probes labeled with fluorescent proteins have been observed in living cells, including endosperm cells of *H. katherinae* (Schmit and Lambert 1990), endosperm cells of *Clivia nobilis* (Endlé et al. 1998), stamen hair cells of *Tradescantia virginiana* (Cleary et al. 1992), and tobacco BY-2 cells (Sano et al. 2005; Yu et al. 2006; Higaki et al. 2008; Maeda et al. 2020). Interestingly, AFs located between the cortical division zone (CDZ) and the phragmoplast guide the edges of cell plates to the CDZ, playing a key role in the formation of the cell plate and selection of the division plane (Kojo et al. 2014; Arima et al. 2018). Thus, AFs regulate the centrifugal growth of the phragmoplast, playing an important role in cytokinesis.

The contribution of phragmoplast AFs to the initial phase of cell plate formation has been increasingly elucidated in recent years although to a considerably lesser extent than their roles in the later stages of cytokinesis. We previously reported that pharmacologic disruption of AFs by actin polymerization inhibitor bistheonellide A leads to malformation of the emerging cell plate in the initial phase of cytokinesis (Higaki et al. 2008). We also found that disruption of AFs by the action of actin polymerization inhibitor latrunculin B (LatB) inhibits the contraction of phragmoplast MTs during the initial phase of cytokinesis, affects the timing of accumulation of NACK1 kinesin, which plays an important role in cell plate expansion, and delays the accumulation of the cell plate membrane (Maeda et al. 2020; Maeda and Higaki 2021). These results suggest that AFs contribute to the proper formation of the cell plate via the contraction of MTs in the initial phragmoplast. Moreover, these studies suggest that AFs are accumulated in the midplane of the mitotic apparatus during the initial phase of cell plate formation, in other words, near the emerging cell plate. However, this has not been clearly verified in previous studies using a probe of AFs, namely the actin-binding domain 2 (ABD2) of AtFIM1 (Sano et al. 2005; Higaki et al. 2008; Maeda et al. 2020), likely because of the limitations of the imaging technique or the fluorescent probe used to label the AFs. Therefore, there is a need to further observe the localization of phragmoplast AFs in the initial phase of cell plate formation.

Precisely capturing the dynamics of phragmoplast AFs in the initial phase of cell plate formation remains challenging. In tobacco BY-2 cells, the progression from phragmoplast formation to expansion occurs within a few minutes (Maeda et al. 2020), necessitating live-cell imaging with high spatiotemporal resolution. However, in confocal laser microscopy, increasing spatiotemporal resolution by increasing the exposure time or shortening the interval of the acquisition time can lead to negative effects, such as significant degradation of fluorescent proteins and cell cycle arrest, owing to excessive laser irradiation (Supplementary Fig. S1). Previous studies have also reported the negative effects of laser irradiation on fluorescent probes, such as photobleaching and phototoxicity, which are related to the exposure time and laser power (Magidson and Khodjakov 2013; Skylaki et al. 2016; Ojha and Ojha 2021). Although minimizing the exposure time and/or laser power reduces the negative effects of light irradiation on the sample, it also reduces the signal-to-noise ratio and degrades spatiotemporal resolution. Therefore, addressing the trade-off between minimizing sample damage and enhancing image quality is critical for detailed investigations of AF dynamics using live-cell imaging.

Here, we explored the possibility of solving this problem computationally. Recently, we demonstrated the effectiveness of deep learning in microscopy image transformation in cell and cytoskeleton segmentation (Kikukawa et al. 2021, 2023; Horiuchi et al. 2024) and virtual staining (Ichita et al. 2025a, b). Building on these advancements, we applied a deep learning-based image restoration technique to enhance the quality of images acquired with short exposure times, enabling live-cell imaging with high spatiotemporal resolution while minimizing sample damage, such as photobleaching and phototoxicity. Using this strategy, we aimed to tackle the challenging task of investigating AF localization during the early stages of cytokinesis.

In this study, we performed three-dimensional time-lapse (4D) imaging of cytokinetic tobacco BY-2 cells using different AF probes, namely Lifeact-RFP and RFP-ABD2, and subsequently, analyzed the data using a deep learning-based image restoration technique. Deep learning-based image restoration enabled us to identify key spatiotemporal regions of interest from comprehensive datasets acquired with high spatiotemporal resolution and reduced cellular damage, namely photobleaching and phototoxicity. We then validated the AF localization patterns indicated by the image restoration results through targeted, long-exposure imaging without the use of deep learning. This direct observation confirmed that the localization of phragmoplast AFs varied depending on the type of fluorescent probe used. Specifically, we found that AFs labeled with Lifeact-RFP, rather than RFP-ABD2, were prominently localized on the midplane of the division apparatus in the initial phase of cell plate formation. These findings support a possible contribution of phragmoplast AFs to the initial phase of cell plate formation.

Materials and methods

Tobacco BY-2 cell culture

Tobacco BY-2 cells (*Nicotiana tabacum* L. cv. Bright Yellow 2) were fluorescently labeled with YFP–β-tubulin (YFP-TUB6), histone H2B–dCFP, and Lifeact–mCherry (Lifeact-RFP) (BY-YTHCLR, Yasuhara and Kitamoto 2014) or YFP–β-tubulin (YFP-TUB6) and red fluorescent protein (tdTomato)-actin-binding domain of the AtFIM1 fusion protein (RFP-ABD2) (BY-YTRF, Kojo et al. 2014) to detect MTs and AFs. Transgenic tobacco BY-2 cells were cultured in modified Linsmaier and Skoog (LS) medium (Nagata et al. 1992). The medium contained the following components: 4.6 g/L Murashige and Skoog plant salt mixture (392–00591, Fujifilm Wako, Osaka, Japan), 30 g/L sucrose (193–00025, Fujifilm Wako), 0.2 g/L potassium dihydrogen phosphate (169–04245, Fujifilm Wako), 0.1 g/L myo-inositol (I5125, Sigma, St. Louis, MO, USA), 1.0 mg/L thiamin hydrochloride (205–00855, Fujifilm Wako), and 0.2 mg/L 2.4-dichlorophenoxyacetic acid (040–18532, Fujifilm Wako). The pH of the medium was adjusted to 5.8 with KOH. The medium was dispensed into 300 mL flasks (95 mL medium/flask). Each flask was capped with aluminum foil and autoclaved at 120 °C for 20 min. Appropriate volumes of BY-2 cell suspension were dispensed into the sterilized medium (1 mL of BY-YTHCLR and 5.5 mL of BY-YTRF) and agitated in a rotary shaker at 130 rpm and 27 °C in the dark. The cell suspension was removed from the flask on day 7 of incubation and transferred to a new flask for subculturing.

Microscopic observation of tobacco BY-2 cells

One day after passaging, transgenic tobacco BY-2 cells were transferred into φ35-mm Petri dishes with φ14-mm coverslip windows at the bottom (Matsunami, Osaka, Japan). The dishes were placed onto the inverted platform of a fluorescence microscope (IX-70; Olympus, Tokyo, Japan) equipped with a CSU-X1 scanning head (Yokogawa, Tokyo, Japan) and a scientific CMOS camera (Prime 95 B; Teledyne Photometrics, Tucson, AZ, USA). YFP was excited with a 488 nm laser and its fluorescence was detected with a 510–550 nm band-pass filter. In contrast, RFP was excited with a 555 nm laser and its fluorescence was detected with a 617–673 nm band-pass filter. The output power of each laser was set to 5% for YFP and 10% for RFP. Images were taken with a silicon-immersion objective lens (60×). The exposure time was adjusted according to the purpose of image acquisition and the fluorescence intensity of transgenic tobacco BY-2 cells.

Microscopic observation of *A. thaliana* zygotes

Zygote imaging was performed using a marker of MTs (EC1p::Clover-TUA6, Horiuchi et al. 2024) and a laser-scanning inverted microscope (AX; Nikon) equipped with a pulse laser (InSight X3 Dual option; Spectra-Physics), as previously described (Kurihara et al. 2017). Fluorescence signals were detected using external non-descanned GaAsP PMT detectors, with a 525/50 nm band-pass filter, 40 × water-immersion objective lens (CFI Apo LWD WI; Nikon), and Immersol W 2010 (Zeiss) immersion medium. Low-, medium-, and high-quality images of the same zygote were acquired by increasing the set laser power 2, 3, and 6 times, respectively.

Acquisition of training image sets of tobacco BY-2 cells and model training

Training image sets were obtained by acquiring images of the same BY-YTHCLR cells at long- and short-exposure times. All images were cropped using ImageJ to create a region of interest (ROI) of 733 × 974 pixels. The pre-processed training images were used to train the image restoration model using image analysis software Aivia (DRVision, Bellevue, WA, USA) (Kikukawa et al. 2021, 2023). "2D Image Restoration" of Aivia was applied to train the model. For image training, a long-exposure image (Example) and a short-exposure image (Raw Data) of the same cell were used as a set. As a result, the model was trained on sets of "2000 and 20 ms images," "2000 and 50 ms images," "2000 and 100 ms images," "2000 and 200 ms images," and "2000 and 200 ms images." The effect of the number of training image sets ($N = 2, 6, 12, 25, 50$, and 100) on image restoration accuracy was examined.

Acquisition of training image sets of *A. thaliana* zygotes and model training

Training image sets were obtained by acquiring images of the same *A. thaliana* zygotes with MTs fluorescently labeled with Clover-TUA6 at high, medium, and low laser powers (see Materials and methods "Microscopic observation of A. thaliana zygotes" for the respective laser power). The training images were used to train the image restoration model using image analysis software Aivia (DRVision). "2D Image Restoration" of Aivia was applied to train the model. For image training, high-quality images (Example)

Fig. 1 Training image sets for image restoration models. A training image set consists of a low-quality image taken with a range of short exposure times and a high-quality image taken with a long exposure time. There are four combination patterns of training image sets: 200 and 2000 ms images, 100 and 2000 ms images, 50 and 2000 ms images, and 20 and 2000 ms images. Scale bar = 40 µm

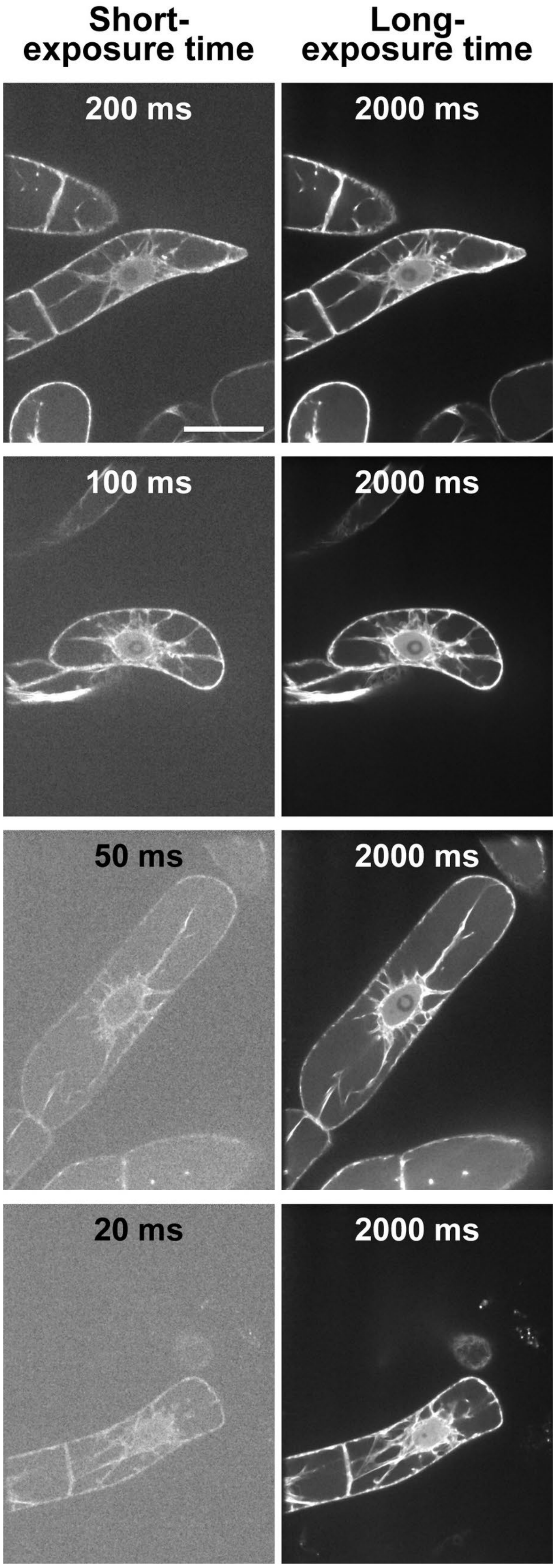

and medium- or low-quality images (Raw Data) of the same zygote were used as sets, and the model was trained for each combination of "high laser power and medium laser power" and "high laser power and low laser power." The number of training image sets was tested with $N = 25$.

Quantitative evaluation of image restoration accuracy

Quantitative evaluation of image restoration accuracy was performed by measuring the signal co-localization and correlation between the long-exposure image and the restored image from the short-exposure image. Specifically, Spearman's rank correlation coefficients for "long-exposure images (2000 ms)" and "images restored from short-exposure images (20, 50, 100, or 200 ms)" were examined using ImageJ plugin EzColocalization (Stauffer et al. 2018).

Three-dimensional (3D) visualization of time-lapse images

3D reconstruction was performed on Z-stack images at selected time points using Amira (Thermo Fisher Scientific, Pittsburgh, PA, USA). Z-stack images used for 3D reconstruction were processed by image restoration for each optical section prior to analysis in Amira. 3D images were visualized using the volume rendering function. GFP and RFP channels were displayed in pseudo color.

Results

The accuracy of image restoration by the model improves in proportion to the quality and number of training images

To investigate the localization of AFs in the initial phragmoplast under conditions of reduced photobleaching and phototoxicity, we decided to train the deep learning-based image restoration model implemented in AIVIA. To achieve this, we systematically evaluated the effects of training image quality and quantity on the accuracy of image restoration. By testing various combinations of image pairs captured with short and long-exposure settings, we aimed to identify the optimal training conditions that balanced improving imaging accuracy with minimizing photobleaching and phototoxicity.

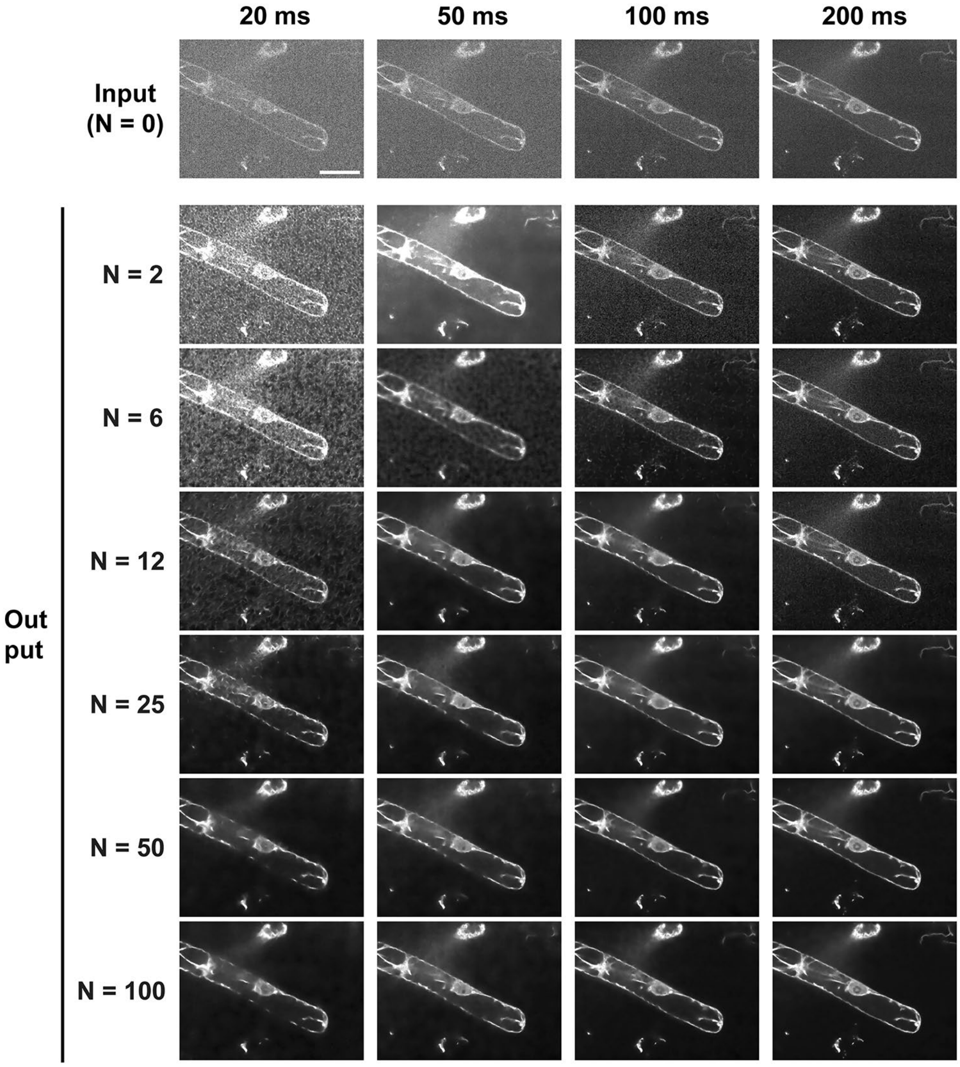

Fig. 2 Effect of the quality and number of training image sets on image restoration. "Input" is images of tobacco BY-2 cells in which actin microfilaments are fluorescently labeled with Lifeact-RFP and taken with the following pattern of exposure times: 20, 50, 100, and 200 ms. "Output" is the result of image restoration performed on images taken with the respective exposure times. *N* indicates the number of training image sets used to train the image restoration model. Scale bar = 40 μm

The long-exposure images (2000 ms) provided high-quality confocal images, while the short-exposure images reduced photobleaching and phototoxicity. This optimization process was crucial for determining the most suitable conditions for subsequent 4D live-cell imaging analysis. To examine the effects of training image quality, we prepared four patterns of training image sets with different short exposure times (Fig. 1). We also examined the effect of the number of training image sets on the model's image restoration accuracy by training several models with different numbers of training image sets. Specifically, we trained 24 models with a combination of four short exposure times (20, 50, 100, and 100 ms) and 6 datasets consisting of different numbers of training image sets (*N* = 2, 6, 12, 25, 50, and 100) to verify the image restoration accuracy.

We then evaluated the image restoration accuracy of the 24 models qualitatively and quantitatively by examining the restoration results of the test images (Figs. 2, 3) (Qualitatively, the image restoration accuracy tended to improve in proportion to the quality and number of training images (Fig. 2). In other words, the detected signals were clearer (relative to the background noise) after image restoration using training images with longer exposure times and models with larger numbers of training image sets. For the quantitative evaluation, Spearman's rank correlation coefficient (SRCC) was calculated to quantify the degree of improvement in similarity to the *ground truth* image (long-exposure image) after image restoration by the model (Fig. 3). The results of the quantitative evaluation were consistent with the results of the qualitative evaluation and showed an improvement in restoration accuracy that was almost proportional to the quality and number of training image sets. Quantitative evaluation by SRCC showed two points: (i) SRCC was lower for relatively low-quality training image sets (20 or 50 ms) than for raw input images when the number of training image sets was very small (*N* = 2) (Fig. 3a, b). This tendency was not observed when the training image sets were of relatively high quality (100 or 200 ms) (Fig. 3c, d).

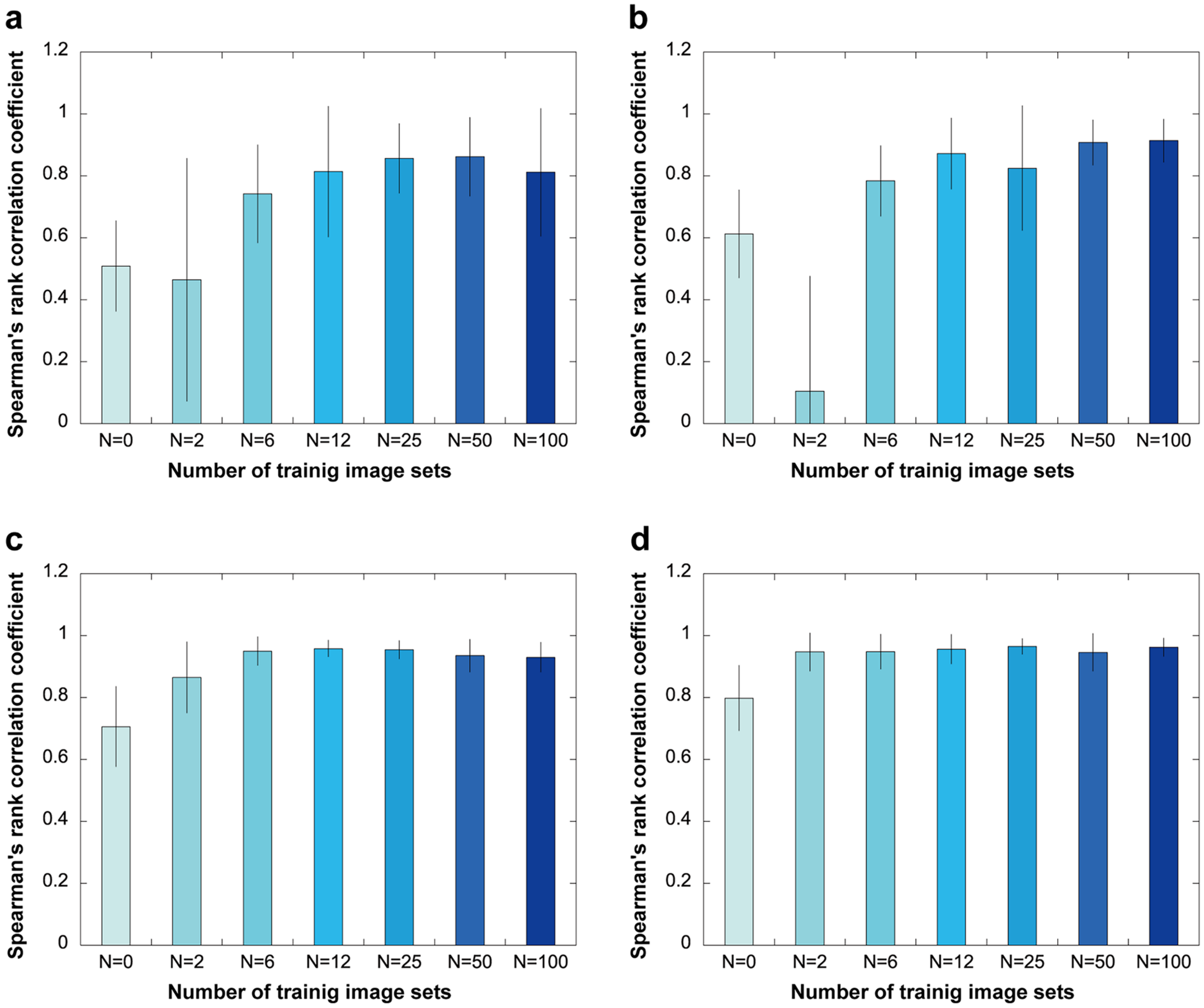

Fig. 3 Quantitative evaluation of the effect of the number of training image sets and input image quality on image restoration accuracy. The results shown are from the quantitative evaluation of image restoration performed on Lifeact-RFP fluorescence images. N indicates the number of training image sets. The input images (N= 0) are taken with four patterns of exposure times: **a** 20, **b** 50, **c** 100, and **d** 200 ms. The input image and the images restored with each model (N= 2, 6, 12, 25, 50, and 100) were compared with the *ground truth* image (taken with a long exposure time of 2000 ms), and their similarity was quantified using Spearman's rank correlation coefficient (SRCC). The vertical axis represents SRCC, with SRCC = 1 indicating high image restoration accuracy. Error bars indicate standard deviation (n= 500 for each bar)

(ii) SRCC was comparable between images restored using relatively low-quality images with the short exposure time of 50 ms and images restored using higher quality input images, if the number of training image sets was sufficient (N= 100) (Fig. 3c, d). Mean and standard deviation (SD) of SRCC for each exposure time (N= 100) were 0.812 ± 0.21 (20 ms), 0.914 ± 0.07 (50 ms), 0.930 ± 0.05 (100 ms), and 0.962 ± 0.03 (200 ms) (Fig. 3). This suggests that image restoration using a model trained with a sufficient number of training image sets can produce images with a quality similar to that of the image taken with a long exposure time (2000 ms), even for a low-quality image taken with a short exposure time of 50 ms. On the basis of the above evaluation results, we used the model trained with the combination of "2000 ms long-exposure image, 50 ms short-exposure image, and N= 100 training image set" for image restoration during the analysis of 4D live-cell images of tobacco BY-2 cells, as described later.

To evaluate the utility of the image restoration technique for bioimaging of plant cells other than tobacco BY-2 cells, we extended the validation of image restoration to fluorescence live-cell imaging of zygotes of a model plant, *A. thaliana* (Supplementary Fig. 2) (Kimata et al. 2016; Hiromoto et al. 2023). The models were trained using pairs of low- and

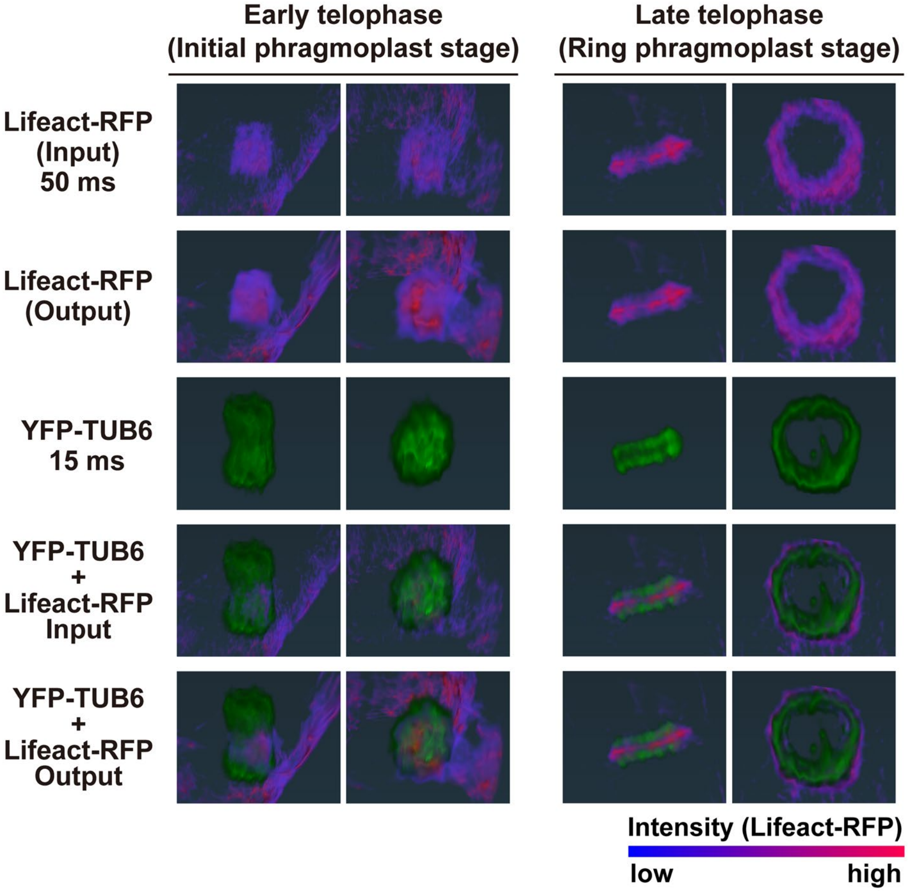

Fig. 4 Effect of image restoration on 4D imaging of tobacco BY-2 cells. Three-dimensional reconstruction of Z-stack images acquired during early telophase and late telophase at the corresponding timepoints. For each phase, the right column shows a vertical view of the cell plate formation plane of the object in the left column. Microtubules labeled with YFP-TUB6 and actin microfilaments labeled with Lifeact-RFP are shown in pseudo colors, with the increase in fluorescence intensity from image restoration indicated by the color map of Lifeact-RFP pseudo colors

high-quality images or medium- and high-quality images of *A. thaliana* zygotes. The quality of each image was determined by the excitation power of the applied laser (detailed acquisition conditions are described in Materials and methods). The model optimized for *A. thaliana* zygotes improved image restoration accuracy both qualitatively and quantitatively (Supplementary Fig. S2). The mean ± SD values of the SRCCs were 0.12 ± 0.02 for input-low, 0.68 ± 0.07 for output-low, 0.20 ± 0.03 for input-medium, 0.70 ± 0.06 for output-low (Supplementary Fig. S2b). For both the low- and medium-quality images, there was a significant improvement in the quality of the output image compared with that of the input image. In other words, the output image was more similar to the *ground truth* high-quality image than the input image (Supplementary Fig. S2).

Image restoration improves the quality of 3D reconstructed images of AFs in tobacco BY-2 cells acquired by low-damage imaging with short exposure times

We then applied the image restoration model to the observation of AF dynamics in the initial phase of cell plate formation (early telophase) and performed 3D reconstruction of Z-stack images at selected time points (Fig. 4). In early telophase, Lifeact-RFP fluorescence was enhanced in the output image (Supplementary Video S1) compared with the input image taken with a short exposure time (50 ms) (Supplementary Video S2). This enhancement confirmed the presence of Lifeact-RFP in the inner region where cell plate formation occurs (Fig. 4, fifth row in early telophase). The signal-to-noise ratio was improved in the output image compared with the input image, making it suitable for 3D structural analysis. Because enhancing the fluorescence signal by increasing the exposure time often leads to photobleaching and phototoxicity (Supplementary Fig. S1), enhancing the fluorescence signal in short-exposure images by image restoration can be a valuable tool in low-damage live-cell observations. In late telophase, the improvement in image quality by image restoration was modest compared with early telophase. The output image showed a slight noise reduction compared with the input image, and it showed a Lifeact-RFP signal localized at the outer edge of the ring-shaped phragmoplast, like the input image (Fig. 4, fourth and fifth row in late telophase).

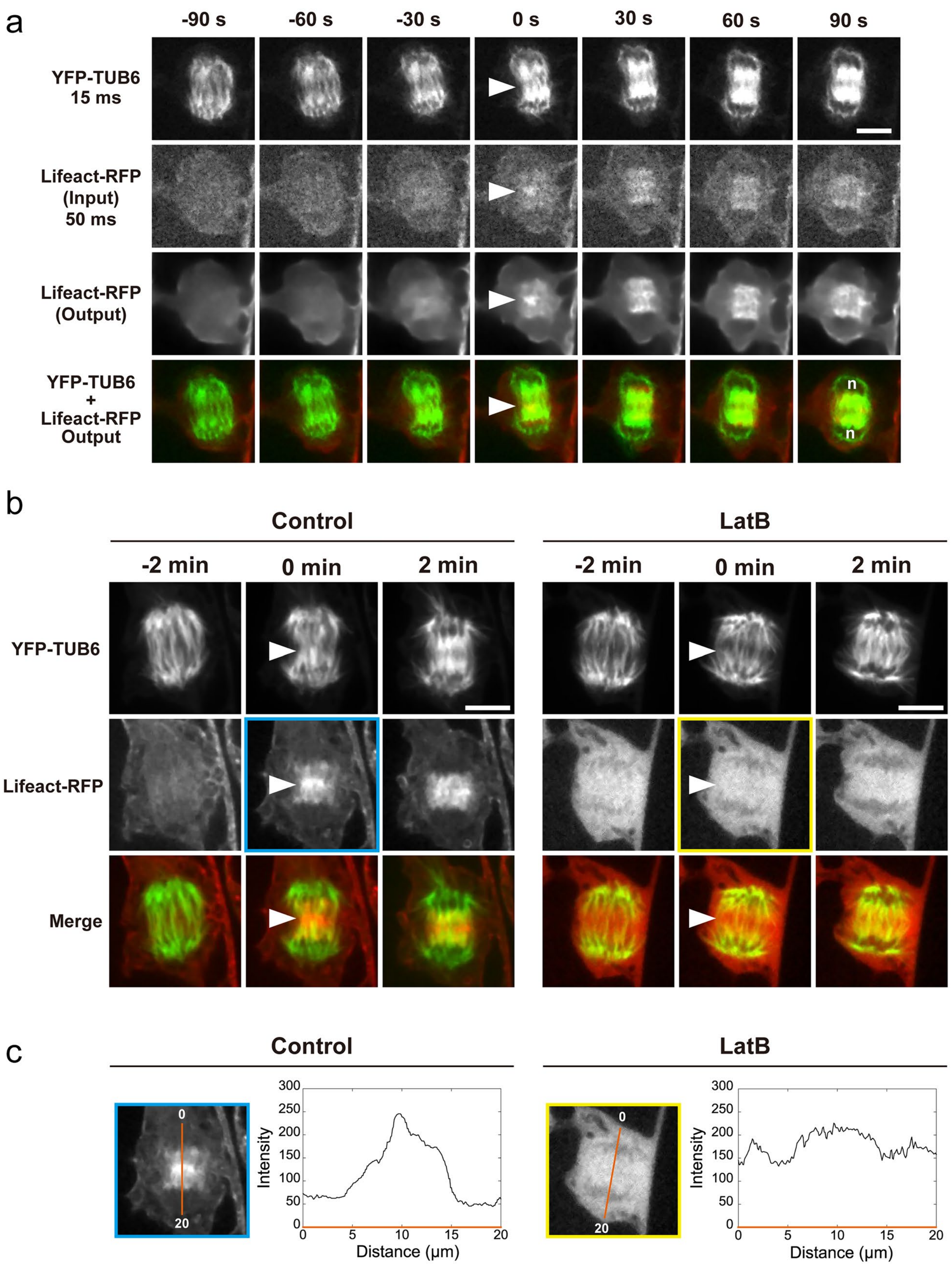
a
-90 s
-60 s
-30 s
0 s
30 s
60 s
90 s
YFP-TUB6 15 ms
Lifeact-RFP (Input) 50 ms
Lifeact-RFP (Output)
YFP-TUB6 + Lifeact-RFP Output
n
n
b
Control
LatB
-2 min
0 min
2 min
-2 min
0 min
2 min
YFP-TUB6
Lifeact-RFP
Merge
c
Control
LatB
0
20
Intensity
300
250
200
150
100
50
0
0
5
10
15
20
Distance (μm)
0
20
Intensity
300
250
200
150
100
50
0
0
5
10
15
20
Distance (μm)

◂**Fig. 5** Application of image restoration to the observation of tobacco BY-2 cells with fluorescently labeled actin microfilaments (Lifeact-RFP) and microtubules (YFP-TUB6). **a** Time-lapse observation using image restoration. n indicates the approximate position of daughter chromosomes. **b** Images taken with a long exposure time. Cells were untreated (Control) or treated with 4 μM Latrunculin B for 1−2 h (LatB) to inhibit actin polymerization. Each time-lapse image is shown with a representative single optical section through the midplane of the division apparatus of 41 (**a**), 8 (**b**, Control), or 7 (**b**, LatB) cells. **c** The intensity profile of Lifeact-RFP at the onset of cell plate formation (0 min in (**b**)) is shown. The intensity changes along the orange line. The time point at the onset of cell plate formation is indicated as 0 min. Arrowheads indicate the initiation region of cell plate formation. Scale bars = 10 μm

Lifeact-RFP-labeled AFs predominately localize near the cell plate during initial stage of formation

To more precisely investigate the localization and dynamics of Lifeact-RFP-labeled AFs during the initial phase of cell plate formation, as indicated by 3D analysis, we examined temporal changes in optical sections through the midplane of the mitotic apparatus (Fig. 5a). Owing to the noise reduction and AF-signal enhancement by image restoration, time-lapse images taken at intervals of 30 s clearly showed the localization of Lifeact-RFP-labeled AFs at the site of cell plate formation (Fig. 5a, arrowheads at 0 s in the third and fourth rows). Lifeact-RFP signals near daughter nuclei were also detected as the cell plate expanded (Fig. 5a, 30–90 s in the third and fourth rows). These time-lapse images are composed of optical sections of Z-stack images acquired at each time point.

Careful examination of the structures of interest found in the restored images is essential because image restoration may produce artifacts from the addition of extra signals or removal of signals from the images. We then checked long-exposure images taken at the same phase (or initial phase of cell plate formation) (Fig. 5b). It should be noted that long-term time-lapse imaging with long exposure times results in cell cycle arrest owing to phototoxicity and fading of the fluorescence signal owing to photobleaching (Supplementary Fig. S1). Therefore, we performed long-exposure imaging at 3–5 timepoints in the phase of interest, which were pre-determined by observations using image restoration. Because the Z-stack images were acquired with long exposure times, the shortest interval was 2 min. These time-lapse images provided optical sections through the midplane of the mitotic apparatus (Fig. 5b). AF localization at the site of cell plate formation was directly observed in the long-exposure images, confirming that AF localization inferred through image restoration corresponded to actual structures (Fig. 5a, b, Control).

We also tested the inhibition of actin polymerization by LatB treatment to verify whether the signal of Lifeact-RFP-labeled AFs detected at the site of cell plate formation was derived from AFs (Fig. 5b, LatB). After 1−2 h of LatB treatment, the Lifeact-RFP signal was diffused around the mitotic apparatus, indicating that actin polymerization was inhibited (Fig. 5b, LatB). Comparison of untreated (Fig. 5b, c (Fig. 5b, c, Control) and LatB-treated (Fig. 5b, c, LatB) groups showed that the signal of Lifeact-RFP-labeled AFs at the site of cell plate formation was indeed derived from AFs.

Two different probes of AFs, Lifeact-RFP and RFP-ABD2, localize differently during initial stage of cell plate formation

To determine whether AFs labeled with other fluorescent probes exhibit the same localization pattern and dynamics as AFs labeled with Lifeact-RFP, tobacco BY-2 cells were fluorescently labeled with RFP-ABD2 and analyzed. The sequence of the analysis was identical to that for Lifeact-RFP-labeled AFs, consisting of time-lapse imaging with image restoration, validation using images taken with long exposure times, and actin polymerization inhibition assays (Fig. 6).

Image restoration of time-lapse images of RFP-ABD2-labeled AFs was performed using the model already established in the previous section (i.e., the model trained on sets of Lifeact-RFP images acquired at 2000 and 50 ms). As shown in Fig. 6a, the model trained on Lifeact-RFP images successfully improved the quality of time-lapse images of RFP-ABD2-labeled AFs (Fig. 6a, second and third rows). Time-lapse images with image restoration showed that RFP-ABD2-labeled AFs rarely localized near the cell plate in the early stage of plate formation (Fig. 6a, 0 s in third and fourth rows) but localized near the daughter nuclei as the cell plate expanded (Fig. 6a, 30–90 s in the third and fourth rows). This observation is consistent with previous reports (Higaki et al. 2008; Maeda et al. 2020).

Time-lapse images of RFP-ABD2-labeled AFs acquired with long exposure times supported the localization pattern detected by image restoration as in the case of Lifeact-RFP (Fig. 6b, Control). In addition, inhibition of actin polymerization by LatB treatment disturbed the localization pattern of RFP-ABD2-labeled AFs (Fig. 6b, c). Taken together, our results showed that image restoration revealed accurate dynamics of AFs, even in the case of RFP-ABD2-labeled AFs, shedding light on the differences in the dynamics of AFs labeled with Lifeact-RFP and RFP-ABD2 (Fig. 7).

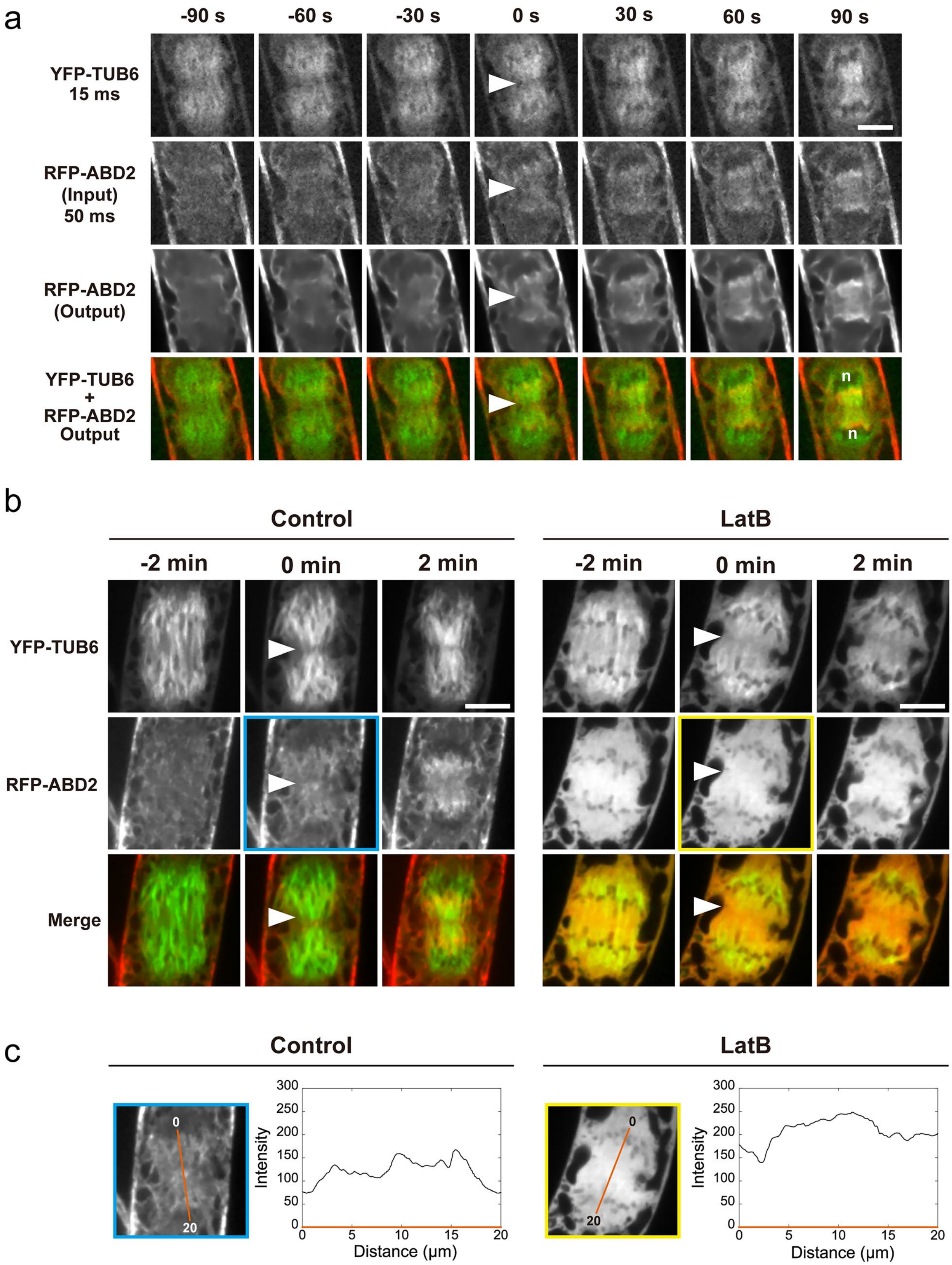
a
-90 s
-60 s
-30 s
0 s
30 s
60 s
90 s
YFP-TUB6 15 ms
RFP-ABD2 (Input) 50 ms
RFP-ABD2 (Output)
YFP-TUB6 + RFP-ABD2 Output
n
n
b
Control
LatB
-2 min
0 min
2 min
-2 min
0 min
2 min
YFP-TUB6
RFP-ABD2
Merge
c
Control
LatB
0
20
Intensity
300
250
200
150
100
50
0
0
5
10
15
20
Distance (µm)
0
20
Intensity
300
250
200
150
100
50
0
0
5
10
15
20
Distance (µm)

◂**Fig. 6** Application of image restoration to the observation of tobacco BY-2 cells with fluorescently labeled actin microfilaments (RFP-ABD2) and microtubules (YFP-TUB6). **a** Time-lapse observation using image restoration. n indicates the approximate position of daughter chromosomes. **b** Images taken with a long exposure time. Cells were untreated (Control) or treated with 4 µM Latrunculin B for 1−2 h (LatB) to inhibit actin polymerization. Each time-lapse image is shown with a representative single optical section through the midplane of the division apparatus of 36 (**a**) or 14 (**b**, Control), or 6 (**b**, LatB) cells. **c** The intensity profile of RFP-ABD2 at the onset of cell plate formation (0 min in (**b**)) is shown. The intensity changes along the orange line. The time point at the onset of cell plate formation is indicated as 0 min. Arrowheads indicate the initiation region of cell plate formation. Scale bars = 10 µm

Discussion

Image restoration is an effective tool for reducing the negative effects of laser exposure and improving spatiotemporal resolution in live-cell imaging of tobacco BY-2 cells

In this study, we applied deep learning-based image restoration models to improve the quality of fluorescent images of AFs in tobacco BY-2 cells during cell division. Deep learning has several advantages for image restoration in live-cell imaging. Deep learning algorithms can effectively remove various features degrading images, such as noise, blur, and artifacts, resulting in clearer and more accurate images (Belthangady and Royer 2019). Additionally, deep learning-based image restoration can be easily applied to different imaging modalities and datasets, making them versatile and adaptable to various research needs (Jin et al. 2020; Huang et al. 2023; Ma et al. 2024). In fact, deep learning-based image restoration has recently been used to improve the spatiotemporal resolution of fluorescence live-cell imaging (Weigert et al. 2018; Wang et al. 2019; Laine et al. 2021). Because this technology enhances the weak signals buried in noise, laser exposure can be minimized during imaging (Chen et al. 2020; Laine et al. 2021; Boothe et al. 2023; Ma et al. 2024). However, there are also some disadvantages to using deep learning for image restoration. Deep learning algorithms heavily rely on training data, and the quality and the diversity of the training dataset can significantly impact the performance of the restoration model (Belthangady and Royer 2019). It is often difficult to experimentally acquire large numbers of appropriate training image sets (low- and high-quality image pairs), which is also an obstacle to the practical application of deep learning-based fluorescence image restoration. Moreover, deep learning models applied to extremely noisy images may introduce artifacts or deceiving results, which affects the accuracy of quantitative measurements and tracking results (Belthangady and Royer 2019). Hence, we qualitatively and quantitatively evaluated the accuracy of the image restoration method used (Figs. 2, 3), as described below.

Our qualitative and quantitative evaluations revealed that the quality and the number of training image sets are associated with image restoration accuracy (Figs. 2, 3). It is interesting to note that using a model trained on 100 image sets to restore an image taken with an exposure time of 50 ms produced an output image that was similar to the *ground truth* image acquired with an exposure time of 2000 ms (Fig. 3b). Features of AFs labeled with Lifeact-RFP or RFP-ABD2, as indicated by image restoration, also existed in images taken with a long exposure time (Fig. 5, 6). Thus, our image restoration model enabled high-resolution live-cell imaging with reduced exposure times, from 2000 to 50 ms, minimizing damage to tobacco BY-2 cells. Moreover, the image restoration model was trained on a relatively small number of image sets using the pre-trained model in AIVIA, demonstrating the potential to apply image restoration to the observation of objects for which a large number of training image sets was difficult to acquire. It should be noted that the accuracy of restoring short-exposure images decreased significantly when the number of training image sets was extremely small (Fig. 3a, b; number of training image sets = 2, exposure time of input images = 20 and 50 ms), which may be related to artifacts arising from noisy features in the training images, as described in previous studies (Belthangady and Royer 2019).

Limitations and potential applications of image restoration in this study

This study expands the potential use of image restoration models in biologic research, particularly in live-cell imaging of plants. However, it should be noted that acquiring a suitable image set for training the image restoration model is a major limiting factor. That is, when acquiring high- and low-quality image sets, if the positions of the objects of interest in the images do not match, the accuracy of the model after training will significantly degrade. This problem is critical when acquiring training image sets of models focusing on intracellular structures that rapidly change their shape.

Future applications of image restoration include exploratory observations of unknown intracellular phenomena. Although long-term live-cell imaging with short acquisition intervals is effective for detecting the dynamics of novel and interest intracellular structures, it is difficult to conduct in practice owing to the negative effects of prolonged observation, namely phototoxicity and photobleaching (Magidson and Khodjakov 2013; Skylaki et al. 2016; Ojha and Ojha 2021). This study showed that image restoration enabled live-cell imaging with reduced phototoxicity (e.g., cell cycle arrest) and photobleaching (Supplementary Fig. S1), paving the way for long-term live-cell fluorescence imaging with reduced cellular damage. This positions our image restoration approach alongside optical approaches that minimize

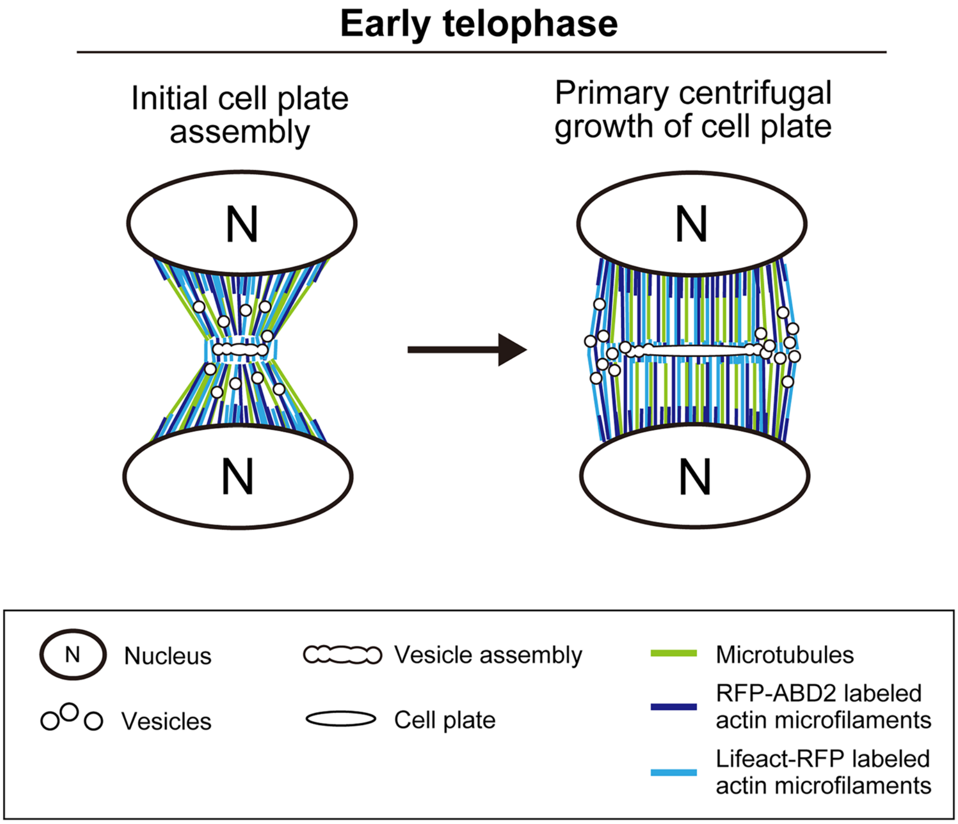

Fig. 7 Schematic diagram of actin microfilament dynamics during early telophase. Lifeact-RFP- and RFP-ABD2-labeled actin microfilaments localized around the cell plate initiation region and daughter nuclei during initial cell plate assembly, to different levels. The vesicle assembly region was dominated by Lifeact-RFP labeled actin microfilaments, with few or absent RFP-ABD2-labeled actin microfilaments. During primary centrifugal growth of the cell plate or phragmoplast expansion, Lifeact-RFP labeled actin microfilaments were highly co-localized with microtubules of the phragmoplast and localized around the forming cell plate, while RFP-ABD2-labeled actin microfilaments were highly localized near the daughter nuclei

laser exposure, such as light sheet microscopy and lattice light sheet microscopy (Daetwyler and Fiolka 2023; Sinclair et al. 2024). High-resolution 4D live-cell imaging with reduced cellular damage using image restoration also enables the detection of various biologic events for insights into cellular workings. Our image restoration approach was applicable to live-cell imaging of not only tobacco BY-2 cells but also *A. thaliana* zygotes (Supplementary Fig. S2), suggesting that it could be applied to study a wide range of plant species, cell types, and organelles if suitable training images are available.

Differences in the dynamics of AFs labeled with different probes in the initial phase of cell plate formation

Analyzing 4D images of tobacco BY-2 cells using our image restoration technique revealed that the dynamics of AFs in the initial phase of cell plate formation differed depending on the attached probe. The observed localization differences between ABD2-labeled and Lifeact-labeled AFs could be due to probe-induced artifacts rather than biologic differences (van der Honing et al. 2011). However, this possibility does not fully explain our observations. The vesicle assembly region was dominated by Lifeact-RFP-labeled AFs, with little or absent RFP-ABD2-labeled AFs, which were predominately localized near the daughter nuclei (Figs. 5, 6, 7). Previous studies reported that AFs are involved in the initial phase of cell plate formation (Higaki et al. 2008; Maeda et al. 2020; Maeda and Higaki 2021). The different dynamics of Lifeact-RFP-labeled AFs and RFP-ABD2-labeled AFs suggest that specific types of AFs are involved in vesicle trafficking during cell plate formation (Figs. 5, 6, 7).

The difference in dynamics between Lifeact-RFP-labeled AFs and RFP-ABD2-labeled-AFs may be understood by considering the respective properties of Lifeact and ABD2. ABD2 fused with fluorescent proteins has been used to visualize the dynamic organization of AFs in vivo, providing detailed structural insights (Sheahan et al. 2004; Wang et al. 2008; Higaki et al. 2008; Maeda et al. 2020). Lifeact, a peptide consisting of the first 17 amino acids of yeast protein Abp140, has been used to clearly visualize filamentous AFs in eukaryotic cells and tissues. (Riedl et al. 2008). Previous studies have shown that Lifeact is an excellent probe for studying AF organization and dynamics in plants because, when expressed to the correct level, it labels AF populations such as thin F-actin, which are undetectable with ABD2 as the AF marker (van der Honing et al. 2011). However, certain native AFs of plant cells may remain unaffected by Lifeact because a number of AtACT2-containing filaments in *Nicotiana benthamiana* leaf epidermal cells do not interact with Lifeact (Kijima et al. 2018). Moreover, different actin isoforms can build their own filament arrays depending on the cell and tissue type, and selective visualization of each filament array is possible depending on the type of actin-binding protein, as proposed by Kijima et al. (2018). Considering the above studies, it is possible that AFs specifically labeled with Lifeact-RFP, rather than RFP-ABD2, regulate vesicle arrays in situ in the initial phase of cell plate formation. Actin polymerization inhibition tests with LatB showed that the midzone contraction of the anaphase spindle is inhibited in the initial stage of cell plate formation (Maeda et al. 2020), which may be attributed to the absence of Lifeact-RFP-labeled AFs around the midzone and the failure of MT guidance. Future studies focusing on the differential dynamics of Lifeact-RFP- and RFP-ABD2-labeled AFs will provide a deeper understanding of the role of AFs in cell plate formation.

Supplementary Information The online version contains supplementary material available at https://doi.org/10.1007/s00299-025-03498-7.

Acknowledgements We thank Ms. Hitomi Okada (Kumamoto University) and Ms. Remi Kawakami (Kumamoto University) for their support in cell culture maintenance. We thank Edanz (https://jp.edanz.com/ac) for editing a draft of this manuscript.

Author contributions Takumi Higaki conceived and designed the experiments. Suzuka Kikuchi, Takumi Kotaka, and Takumi Higaki performed 4D imaging analysis using the image restoration model. Yuga Hanaki and Minako Ueda acquired the image of *A. thaliana* zygotes. Suzuka Kikuchi and Takumi Higaki wrote the manuscript, and all authors participated in the discussion and review of the manuscript.

Funding Open Access funding provided by Kumamoto University. This work was supported by the Japan Science and Technology Agency (CREST; JPMJCR2121) to Takumi Higaki and Minako Ueda; Japan Society for the Promotion of Science [Advanced Bioimaging Support (JP22H04926 to Minako Ueda), International Leading Research KEPLR (JP22 K21352 to Minako Ueda) and a Grant-in-Aid for Scientific Research (B) (JP23H02494 to Minako Ueda)]; and Suntory Rising Stars Encouragement Program in Life Sciences (SunRiSE; to Minako Ueda).

Data availability All relevant data are available from the authors on reasonable request.

Declarations

Conflict of interest The authors declare that the research was conducted in the absence of any commercial or financial relationships that could be construed as a potential conflict of interest.

References

Arima K, Tamaoki D, Mineyuki Y et al (2018) Displacement of the mitotic apparatuses by centrifugation reveals cortical actin organization during cytokinesis in cultured tobacco BY-2 cells. J Plant Res 131:803–815. https://doi.org/10.1007/s10265-018-1047-4

Belthangady C, Royer LA (2019) Applications, promises, and pitfalls of deep learning for fluorescence image reconstruction. Nat Methods 16:1215–1225. https://doi.org/10.1038/s41592-019-0458-z

Boothe T, Ivanković M, Grohme MA et al (2023) Content aware image restoration improves spatiotemporal resolution in luminescence imaging. Commun Biol 6:1–7. https://doi.org/10.1038/s42003-023-04886-z

Chen F, Liu J, Gou D et al (2020) An accurate and universal approach for short-exposure-time microscopy image enhancement. Comput Med Imaging Graph 83:101743. https://doi.org/10.1016/j.compmedimag.2020.101743

Clayton L, Lloyd CW (1985) Actin organization during the cell cycle in meristematic plant cells: actin is present in the cytokinetic phragmoplast. Exp Cell Res 156:231–238. https://doi.org/10.1016/0014-4827(85)90277-0

Cleary AL, Gunning BES, Wasteneys GO, Hepler PK (1992) Microtubule and F-actin dynamics at the division site in living *Tradescantia* stamen hair cells. J Cell Sci 103:977–988. https://doi.org/10.1242/jcs.103.4.977

Daetwyler S, Fiolka RP (2023) Light-sheets and smart microscopy, an exciting future is dawning. Commun Biol 6:1–11. https://doi.org/10.1038/s42003-023-04857-4

Endlé M-C, Stoppin V, Lambert A-M, Schmit A-C (1998) The growing cell plate of higher plants is a site of both actin assembly and vinculin-like antigen recruitment. Eur J Cell Biol 77:10–18. https://doi.org/10.1016/S0171-9335(98)80097-6

Hasezawa S, Marc J, Palevitz BA (1991) Microtubule reorganization during the cell cycle in synchronized BY-2 tobacco suspensions. Cell Motil 18:94–106. https://doi.org/10.1002/cm.970180204

Higaki T, Kutsuna N, Sano T, Hasezawa S (2008) Quantitative analysis of changes in actin microfilament contribution to cell plate development in plant cytokinesis. BMC Plant Biol 8:80. https://doi.org/10.1186/1471-2229-8-80

Hiromoto Y, Minamino N, Kikuchi S et al (2023) Comprehensive and quantitative analysis of intracellular structure polarization at the apical–basal axis in elongating *Arabidopsis* zygotes. Sci Rep 13:22879. https://doi.org/10.1038/s41598-023-50020-8

Horiuchi R, Kamimura A, Hanaki Y et al (2024) Deep learning-based cytoskeleton segmentation for accurate high-throughput measurement of cytoskeleton density. Protoplasma. https://doi.org/10.1007/s00709-024-02019-9

Huang B, Li J, Yao B et al (2023) Enhancing image resolution of confocal fluorescence microscopy with deep learning. PhotoniX 4:2. https://doi.org/10.1186/s43074-022-00077-x

Ichita M, Horiuchi R, Higaki T (2025a) Expanding plant cell microscopy through artificial intelligence focusing on segmentation and virtual staining. Cytologia (in press).

Ichita M, Yamamichi H, Higaki T (2025b) Virtual staining from bright-field microscopy for label-free quantitative analysis of plant cell structures. Plant Mol Biol 115:29. https://doi.org/10.1007/s11103-025-01558-w

Jin L, Liu B, Zhao F et al (2020) Deep learning enables structured illumination microscopy with low light levels and enhanced speed. Nat Commun 11:1934. https://doi.org/10.1038/s41467-020-15784-x

Jürgens G (2005) Cytokinesis in higher plants. Ann Rev Plant Biol 56:281–299. https://doi.org/10.1146/annurev.arplant.55.031903.141636

Kakimoto T, Shibaoka H (1987) Actin filaments and microtubules in the preprophase band and phragmoplast of tobacco cells. Protoplasma 140:151–156. https://doi.org/10.1007/BF01273724

Kijima ST, Staiger CJ, Katoh K et al (2018) *Arabidopsis* vegetative actin isoforms, AtACT2 and AtACT7, generate distinct filament arrays in living plant cells. Sci Rep 8:4381. https://doi.org/10.1038/s41598-018-22707-w

Kikukawa K, Yoshimura K, Watanabe A, Higaki T (2021) Metal-nano-ink coating for monitoring and quantification of cotyledon epidermal cell morphogenesis. Front Plant Sci. https://doi.org/10.3389/fpls.2021.745980

Kikukawa K, Takigawa-Imamura H, Soga K et al (2023) Smooth elongation of pavement cells induced by RIC1 overexpression leads to marginal protrusions of the cotyledon in *Arabidopsis thaliana*. Plant Cell Physiol 64:1356–1371. https://doi.org/10.1093/pcp/pcad094

Kimata Y, Higaki T, Kawashima T et al (2016) Cytoskeleton dynamics control the first asymmetric cell division in *Arabidopsis* zygote. PNAS 113:14157–14162. https://doi.org/10.1073/pnas.1613979113

Kojo KH, Yasuhara H, Hasezawa S (2014) Time-sequential observation of spindle and phragmoplast orientation in BY-2 cells with altered cortical actin microfilament patterning. Plant Signal Behav 9:e29579. https://doi.org/10.4161/psb.29579

Kurihara D, Kimata Y, Higashiyama T, Ueda M (2017) In vitro ovule cultivation for live-cell imaging of zygote polarization and embryo patterning in *Arabidopsis thaliana*. J vis Exp. https://doi.org/10.3791/55975

Laine RF, Jacquemet G, Krull A (2021) Imaging in focus: an introduction to denoising bioimages in the era of deep learning. Int J Biochem Cell Biol 140:106077. https://doi.org/10.1016/j.biocel.2021.106077

Li Y, Shen Y, Cai C et al (2010) The type II *Arabidopsis* Formin14 interacts with microtubules and microfilaments to regulate cell division. Plant Cell 22:2710–2726. https://doi.org/10.1105/tpc.110.075507

Livanos P, Müller S (2019) Division plane establishment and cytokinesis. Ann Rev Plant Biol 70:239–267. https://doi.org/10.1146/annurev-arplant-050718-100444

Ma C, Tan W, He R, Yan B (2024) Pretraining a foundation model for generalizable fluorescence microscopy-based image restoration. Nat Methods. https://doi.org/10.1038/s41592-024-02244-3

Maeda K, Higaki T (2021) Disruption of actin filaments delays accumulation of cell plate membranes after chromosome separation. Plant Signal Behav 16:1873586. https://doi.org/10.1080/15592324.2021.1873586

Maeda K, Sasabe M, Hanamata S et al (2020) Actin filament disruption alters phragmoplast microtubule dynamics during the initial phase of plant cytokinesis. Plant Cell Physiol 61:445–456. https://doi.org/10.1093/pcp/pcaa003

Magidson V, Khodjakov A (2013) Circumventing photodamage in live-cell microscopy. Methods Cell Biol 114:545–560. https://doi.org/10.1016/B978-0-12-407761-4.00023-3

Müller S, Jürgens G (2016) Plant cytokinesis—no ring, no constriction but centrifugal construction of the partitioning membrane. Semin Cell Dev Biol 53:10–18. https://doi.org/10.1016/j.semcdb.2015.10.037

Nagata T, Nemoto Y, Hasezawa S (1992) Tobacco BY-2 cell line as the “HeLa” cell in the cell biology of higher plants. In: Jeon KW, Friedlander M (eds) International review of cytology. Academic Press, Cambridge, pp 1–30

Ojha A, Ojha NK (2021) Excitation light-induced phototoxicity during fluorescence imaging. J Biosci 46:78. https://doi.org/10.1007/s12038-021-00193-z

Rasmussen CG, Wright AJ, Müller S (2013) The role of the cytoskeleton and associated proteins in determination of the plant cell division plane. Plant J 75:258–269. https://doi.org/10.1111/tpj.12177

Riedl J, Crevenna AH, Kessenbrock K et al (2008) Lifeact: a versatile marker to visualize F-actin. Nat Methods 5:605–607. https://doi.org/10.1038/nmeth.1220

Sano T, Higaki T, Oda Y et al (2005) Appearance of actin microfilament ‘twin peaks’ in mitosis and their function in cell plate formation, as visualized in tobacco BY-2 cells expressing GFP–fimbrin. Plant J 44:595–605. https://doi.org/10.1111/j.1365-313X.2005.02558.x

Schmit AC, Lambert AM (1987) Characterization and dynamics of cytoplasmic F-actin in higher plant endosperm cells during interphase, mitosis, and cytokinesis. J Cell Biol 105:2157–2166. https://doi.org/10.1083/jcb.105.5.2157

Schmit AC, Lambert AM (1990) Microinjected fluorescent phalloidin in vivo reveals the F-actin dynamics and assembly in higher plant mitotic cells. Plant Cell 2:129–138. https://doi.org/10.1105/tpc.2.2.129

Seagull R, Falconer M, Weerdenburg C (1987) Microfilaments: dynamic arrays in higher plant cells. J Cell Biol 104:995–1004. https://doi.org/10.1083/jcb.104.4.995

Sheahan MB, Staiger CJ, Rose RJ, McCurdy DW (2004) A green fluorescent protein fusion to actin-binding domain 2 of *Arabidopsis* Fimbrin highlights new features of a dynamic actin cytoskeleton in live plant cells. Plant Physiol 136:3968–3978. https://doi.org/10.1104/pp.104.049411

Sinclair R, Wang M, Jawaid MZ et al (2024) Four-dimensional quantitative analysis of cell plate development in *Arabidopsis* using lattice light sheet microscopy identifies robust transition points between growth phases. J Exp Bot 75:2829–2847. https://doi.org/10.1093/jxb/erae091

Skylaki S, Hilsenbeck O, Schroeder T (2016) Challenges in long-term imaging and quantification of single-cell dynamics. Nat Biotechnol 34:1137–1144. https://doi.org/10.1038/nbt.3713

Smertenko A (2018) Phragmoplast expansion: the four-stroke engine that powers plant cytokinesis. Curr Opin Plant Biol 46:130–137. https://doi.org/10.1016/j.pbi.2018.07.011

Smertenko A, Assaad F, Baluška F et al (2017) Plant cytokinesis: terminology for structures and processes. Trends Cell Biol 27:885–894. https://doi.org/10.1016/j.tcb.2017.08.008

Stauffer W, Sheng H, Lim HN (2018) EzColocalization: an ImageJ plugin for visualizing and measuring colocalization in cells and organisms. Sci Rep 8:15764. https://doi.org/10.1038/s41598-018-33592-8

Traas JA, Doonan JH, Rawlins DJ et al (1987) An actin network is present in the cytoplasm throughout the cell cycle of carrot cells and associates with the dividing nucleus. J Cell Biol 105:387–395. https://doi.org/10.1083/jcb.105.1.387

van der Honing HS, van Bezouwen LS, Emons AMC, Ketelaar T (2011) High expression of Lifeact in *Arabidopsis thaliana* reduces dynamic reorganization of actin filaments but does not affect plant development. Cytoskeleton 68:578–587. https://doi.org/10.1002/cm.20534

Wang Y-S, Yoo C-M, Blancaflor EB (2008) Improved imaging of actin filaments in transgenic *Arabidopsis* plants expressing a green fluorescent protein fusion to the C- and N-termini of the fimbrin actin-binding domain 2. New Phytol 177:525–536. https://doi.org/10.1111/j.1469-8137.2007.02261.x

Wang H, Rivenson Y, Jin Y et al (2019) Deep learning enables cross-modality super-resolution in fluorescence microscopy. Nat Methods 16:103–110. https://doi.org/10.1038/s41592-018-0239-0

Weigert M, Schmidt U, Boothe T et al (2018) Content-aware image restoration: pushing the limits of fluorescence microscopy. Nat Methods 15:1090–1097. https://doi.org/10.1038/s41592-018-0216-7

Yasuhara H, Kitamoto K (2014) Aphidicolin-induced nuclear elongation in tobacco BY-2 cells. Plant Cell Physiol 55:913–927. https://doi.org/10.1093/pcp/pcu026

Yu M, Yuan M, Ren H (2006) Visualization of actin cytoskeletal dynamics during the cell cycle in tobacco (*Nicotiana tabacum* L. cv Bright Yellow) cells. Biol Cell 98:295–306. https://doi.org/10.1042/BC20050074